

# Quantum Hall Interferometry in Triangular Domains of Marginally Twisted Bilayer Graphene

Phanibhusan S. Mahapatra,\* Manjari Garg, Bhaskar Ghawri, Aditya Jayaraman, Kenji Watanabe, Takashi Taniguchi, Arindam Ghosh, and U. Chandni

Cite This: *Nano Lett.* 2022, 22, 5708–5714

Read Online

ACCESS |

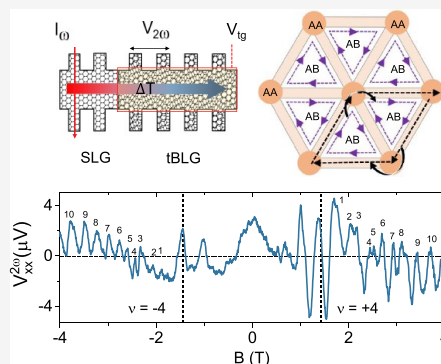
Metrics & More

Article Recommendations

Supporting Information

**ABSTRACT:** Quantum Hall (QH) interferometry provides an archetypal platform for the experimental realization of braiding statistics of fractional QH states. However, the complexity of observing fractional statistics requires phase coherence over the length of the interferometer, as well as suppression of Coulomb charging energy. Here, we demonstrate a new type of QH interferometer based on marginally twisted bilayer graphene (mtBLG), with a twist angle  $\theta \approx 0.16^\circ$ . With the device operating in the QH regime, we observe distinct signatures of electronic Fabry–Pérot and Aharonov–Bohm oscillations of the magneto-thermopower in the density–magnetic field phase space, at Landau level filling factors  $\nu = 4, 8$ . We find that QH interference effects are intrinsic to the triangular AB/BA domains in mtBLG that show diminished Coulomb charging effects. Our results demonstrate phase-coherent interference of QH edge modes without any additional gate-defined complex architecture, which may be beneficial in experimental realizations of non-Abelian braiding statistics.

**KEYWORDS:** Twisted bilayer graphene, Seebeck effect, Quantum Hall interferometry, Fabry–Pérot interference, Aharonov–Bohm interference



The interference between edge modes in integer and fractional quantum Hall (QH) regimes can be used to directly probe the underlying hierarchy of the quasiparticle excitations.<sup>1–9</sup> Intriguingly, this proposal can be particularly effective in observing the non-Abelian braiding statistics of quasiparticles in the fractional QH regime.<sup>3,4</sup> The difficulty in experimental realizations of such phenomena involves the inevitable Coulomb repulsion from the confined quasiparticles, which changes the effective area of the interferometer.<sup>10,11</sup> This additional charging effect is detrimental to observing robust braiding statistics, which can be somewhat mitigated by larger device dimensions, albeit at the expense of phase coherence between the interfering paths.<sup>12</sup> This has led to various device architectures,<sup>13–18</sup> and materials engineering<sup>3</sup> to suppress the Coulomb repulsion, while maintaining the phase coherence of the quasiparticles.

Here, we report the operation of a new type of QH interferometer based on a marginally twisted bilayer graphene (mtBLG) device at  $\theta \approx 0.16^\circ$ . The moiré lattice and the corresponding band structure of tBLG at or near the magic angle ( $\theta_m = 1.1^\circ$ ) can host a myriad of novel phases such as correlated insulators,<sup>19</sup> superconductivity,<sup>20</sup> and magnetism.<sup>21</sup> When the twist angle is well below  $\theta_m$ , relaxation effects change the atomic registries of the moiré lattice.<sup>22</sup> This leads to a mosaic structure of triangular regions consisting of alternate AB and BA stacking, which are separated by domain walls (Figure 1a). When a vertical displacement field gaps out the

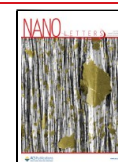
AB/BA regions, the domain walls can host a topologically protected helical one-dimensional (1D) network of conducting channels.<sup>23–26</sup> The quasiparticle transport through the helical 1D network can support AhB-oscillations when subjected to a perpendicular magnetic field.<sup>27</sup> However, in previous reports<sup>27,28</sup> the helical 1D network remained insensitive to the QH phenomenon because the bulk AB/BA regions were depleted of charge carriers.

In this paper, we have performed electrical and thermoelectric measurements in mtBLG with  $\theta \approx 0.16^\circ$  in the integer QH regime at negligible displacement fields. The thermoelectric coefficient provides a fundamental characterization of the electronic state because the diffusive nature of the transport is characteristically sensitive to the scattering dynamics of the charge carriers.<sup>29,30</sup> Furthermore, in the QH regime, the entropy is carried by the quasiparticle excitations instead of the edge modes. Because the entropy flow can be probed by the thermal response of the system, magneto-thermopower can provide a direct insight into the quasiparticle spectrum in a QH regime.<sup>31,32</sup> Under appropriate conditions, the statistical

Received: February 16, 2022

Revised: June 28, 2022

Published: July 7, 2022



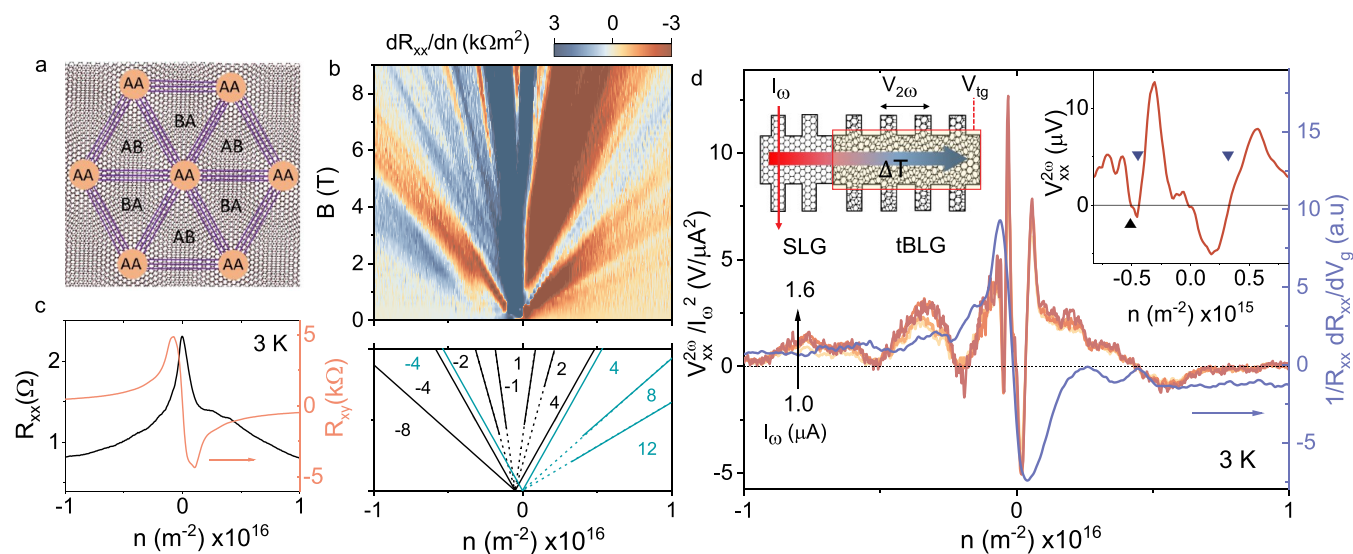


**Figure 1.** Magneto-resistance and thermopower measurements. (a) The AB/BA triangular domains in mtBLG separated by AA-stacked regions and domain walls. (b) Landau fan diagram of four terminal resistance ( $R_{xx}$ ). Measurements are taken at 3 K. The bottom panel shows the reconstructed Landau level structure with filling factors ( $\nu$ ). The green lines show the Landau fan emanating from the CNP, while the black lines show the secondary Landau fans emanating from the full-filling of the first moiré band on the hole-doping side. (c) Doping dependence of  $R_{xx}$  at  $B = 0$  and Hall resistance ( $R_{xy}$ ) at 800 mT. (d) Doping dependence of Seebeck voltage  $V_{xx}^{2\omega}$  normalized with  $I_{2\omega}^2$ , for a range of  $I_{2\omega}$ , at 3 K. The blue curve shows  $\gamma = (1/R_{xx}) dR_{xx}/dV_{tg}$  for comparison on the right axis. The left inset illustrates the measurement schematic for thermopower. The right inset shows the magnified part of  $V_{xx}^{2\omega}$  near the CNP, where blue markers show the van Hove singularities (vHs) and the full-filling of the first moiré band (black marker).

properties of the non-Abelian quasiparticles can also be explored with thermoelectric measurements because the entropy of the anyons is larger compared to that of their Abelian counterparts.<sup>33</sup> Here, we use the dependence of thermal voltage on magnetic field ( $B$ ) and gate-induced density ( $n$ ) to probe the diverse characteristics of interference effects in the QH regime.

The twist angle of the measured tBLG device (see Supporting Information for device geometry and fabrication details) is estimated from the Hofstadter butterfly pattern of  $dR_{xx}/dn$  at 3 K (Figure 1b), where the primary Landau levels (LL) emerge from the charge neutrality point (CNP) (green lines) at  $n = 0$  while on the hole-doped side, another set of LLs emerge (black dashed lines) from  $n_s = 5 \times 10^{14} \text{ m}^{-2}$ .<sup>34</sup> The secondary LLs account for the filling of the first miniband of the moiré lattice. We derive the moiré period  $\lambda \approx 92 \text{ nm}$  from  $n_s$ , with a corresponding twist angle  $\theta \approx 0.16^\circ$ . The primary LLs originating from the CNP exhibit the filling factor sequence  $\nu = \pm 4, \pm 8, \pm 12$  ( $\nu = n\Phi_0/B$ , where  $\Phi_0 = h/e$  is the magnetic quantum flux). In contrast, the secondary LLs exhibit the distinct QH sequence  $\nu = \pm 1, \pm 2$  for  $B \gtrsim 5 \text{ T}$ . However, the sequence coincides with the 4-fold degeneracy of  $\nu = \pm 4, \pm 8$  at lower magnetic fields. The reduced degeneracy of the QH states at higher magnetic fields clearly indicates the breaking of the spin/valley symmetry, in contrast to the quantum oscillations arising from the CNP. At  $B = 0$ , however, the first miniband shows no distinct peak in  $R_{xx}$ , which has a pronounced maxima only at the CNP (Figure 1c). The absence of resistance maxima near  $\pm n_s$  is possibly because of the presence of a large number of overlapping bands at low energies.<sup>22</sup> This is further supported by the density dependence of  $R_{xy}$  at 800 mT (right axis of Figure 1c), which shows the sign reversal only at the CNP.

To study the thermoelectric transport in mtBLG, we employ local Joule heating in the extended monolayer region by

passing a sinusoidal current ( $I_{\omega}$ ).<sup>29,35</sup> This creates a temperature gradient ( $\Delta T$ ) along the length of the channel (left inset of Figure 1d). The thermoelectric voltage ( $V_{2\omega}$ ) is generated in the second-harmonic ( $2\omega$ ) that is recorded in the tBLG region of the Hall bar ( $x$ -direction) with varying doping and heating currents. The linear response ( $\Delta T \ll T$ ) of the measured  $V_{xx}^{2\omega}$  is verified from  $V_{xx}^{2\omega} \propto I_{\omega}^2$  for the experimental range of heating currents (Figure 1d). As illustrated in Figure 1d, the doping dependence of  $V_{2\omega}$  shows multiple sign reversals when the Fermi energy ( $E_F$ ) is varied across the low-energy band. The sign reversals in  $V_{xx}^{2\omega}$  are usually attributed to changes in the quasi-particle excitations or Fermi surface topology near Lifshitz transitions.<sup>36</sup> The near-symmetric sign change of  $V_{xx}^{2\omega}$  on the both side of the CNP (blue arrows in the right inset of Figure 1d) are attributed to the positions of the van Hove singularities (vHS) in the lowest conduction/valence band of the moiré lattice.<sup>35</sup> On the hole doping side, the additional sign reversal of  $V_{xx}^{2\omega}$  (black arrow in the right inset of Figure 1d) indicates the full-filling of the lowest energy valence band. Assuming filling of four electrons per moiré unit cell, we estimate  $\theta \approx 0.16^\circ$  from the magnitude of  $n_s$ , which matches with the twist-angle estimation from the Hofstadter butterfly in pattern in  $R_{xx}$ .

In the degenerate regime ( $T \ll T_F$ , where  $T_F$  is the Fermi temperature), the density dependence of the in-plane Seebeck coefficient can be obtained from the semiclassical Mott relation<sup>29</sup>

$$S_{\text{Mott}} = \frac{\pi^2 k_B^2 T}{3|e|} \frac{1}{R_{xx}} \frac{dR_{xx}}{dV_{tg}} \frac{dV_{tg}}{dn} \frac{dn}{dE} \Bigg|_{E_F} \quad (1)$$

where  $\gamma = (1/R_{xx}) dR_{xx}/dV_{tg}$  can be measured experimentally, and  $dn/dE$  is the DOS ( $dV_{tg}/dn = e/C_{\text{hBN}}$ , where  $C_{\text{hBN}}$  is the known top-gate capacitance per unit area). Equation 1 indicates that the qualitative features of  $S_{\text{Mott}}$  can be captured

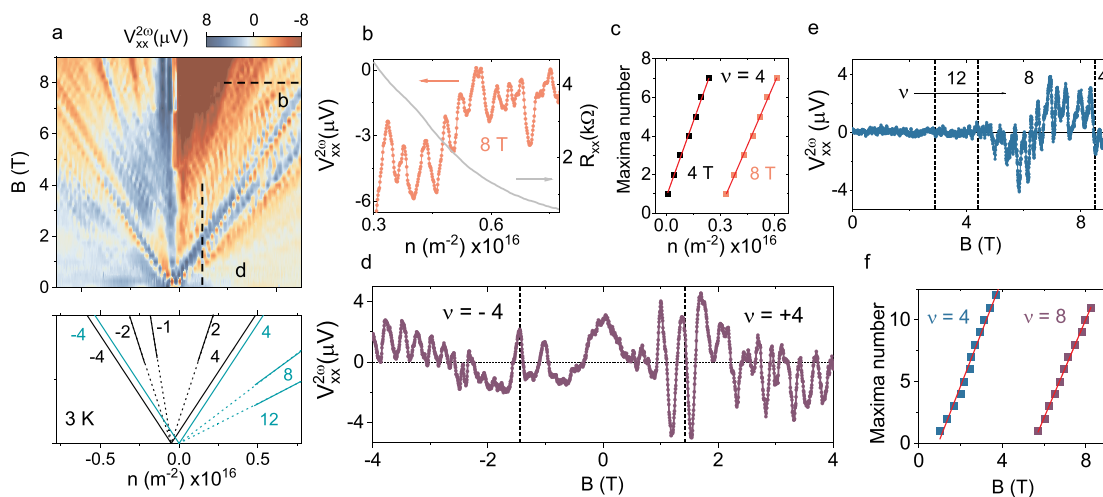


**Figure 2.** Fabry–Pérot (FP) and Aharonov–Bohm (AhB) oscillations in magneto-thermopower. (a) Landau fan diagram of  $V_{xx}^{2\omega}$ . Measurements are taken at 3 K. The bottom panel shows the reconstructed Landau level structure with filling factors ( $\nu$ ). The green lines show the Landau fan emanating from the CNP, while the black lines show the secondary Landau fans emanating from the full-filling of the first moiré band on the hole-doping side. (b) Oscillations in  $V_{xx}^{2\omega}$  (line cut shown by horizontal black dashed lines in panel a) at  $B = 8$  T, while the range of doping is confined to Landau filling  $\nu = 4$ . The right axis shows the density-dependence of  $R_{xx}$  at the same  $B$ . (c) Doping dependence of maxima numbers in thermopower oscillations at  $B = 4$  T and 8 T (for same Landau filling  $\nu = 4$ ), respectively. The red lines show the linear fit. Magnetic field dependence of  $V_{xx}^{2\omega}$  at (d)  $n = 1.55 \times 10^{15} \text{ m}^{-2}$  (vertical line-cut shown in panel a for the positive  $B$  side) and (e)  $n = 7.75 \times 10^{15} \text{ m}^{-2}$ . Value of  $\nu$  is marked with dashed lines. (f)  $B$ -dependence of maxima numbers in thermopower oscillations at  $\nu = 4$  and 8, respectively. The red lines show the linear fit.

by  $\gamma$ , which is compared with normalized  $V_{xx}^{2\omega}$  in the right axis of Figure 1d. However, we find that  $\gamma$  fails to capture the multiple sign changes in  $V_{xx}^{2\omega}$  as  $\gamma$  displays a sign reversal only at the CNP. Notably, the observed discrepancy of signs between  $V_{xx}^{2\omega}$  and  $\gamma$  cannot be compensated by the DOS in eq 1. We speculate that the presence of a large number of vHSs in the DOS of mtBLG can give rise to large anisotropic scattering in the small parts of the Fermi surface that satisfies the Umklapp condition.<sup>37</sup> While this can lead to a violation of the Mott formula, other alternate mechanisms, for instance, correlation effects, can not be entirely ruled out.

Figure 2a shows the Landau fan diagram of thermovoltage  $V_{xx}^{2\omega}$  at 3 K. The  $V_{xx}^{2\omega}$  also exhibits two sets of Landau fans emerging from the CNP and  $n_g$ , with a Landau level sequence that is similar to the Hofstadter butterfly pattern in  $R_{xx}$ . When the device is operated in the QH regime ( $\nu = 4$ ),  $V_{xx}^{2\omega}$  exhibits strong oscillations as a function of  $n$  as shown in Figure 2b. However, such oscillations could not be detected in the conventional  $R_{xx}$  measurements in this regime (right axis in Figure 2b). This indicates a possible role of the entropy current carried by quasiparticle excitations, which can only be detected in the thermal response of the system in the QH regime. While we speculate that the AA nodes in the triangular domains can manifest as compressible regions that can favor the entropy flow over the charge transport,<sup>31,32</sup> the exact mechanism is not clear at present. We find that the oscillations in  $V_{xx}^{2\omega}$  are periodic in  $n$  (Figure 2c). The periodicity  $\Delta n \approx 4 \times 10^{14} \text{ m}^{-2}$  does not vary appreciably when the magnetic field is changed while keeping the filling factor  $\nu$  the same. The periodic oscillations also persist at the higher Landau level  $\nu = 8$  with periodicity  $\Delta n \approx 5 \times 10^{14} \text{ m}^{-2}$ , suggesting that  $\Delta n$  is independent of both  $\nu$  and  $B$ . The periodic oscillations in  $V_{xx}^{2\omega}$  are characteristically similar to the quantum version of the Fabry–Pérot (FP) interferometer for 2D systems, where the cavity is defined by the external gate assembly.<sup>15,28,38</sup> For a cavity length  $L_{\text{cav}}$ , the interference phase in an electronic FP

interferometer is given by  $\phi_e = L_{\text{tot}}k_F/2\pi$ , where  $L_{\text{tot}} = 2L_{\text{cav}}$  is the total path difference between the two interfering trajectories. The phase  $\phi_e$  can be modulated by the changing the energy ( $E_F$ ) of the injected carriers, which in turn changes the wavevector ( $k_F$ ).<sup>39</sup> However, to observe the phase modulation in the presence of a Lorentz force mediated by a magnetic field, the cyclotron radius has to satisfy  $r_c = \hbar k_F/eB > L_{\text{cav}}$ . We estimate  $r_c \approx 9 \text{ nm}$  using the 2D density relation  $k_F = \sqrt{\pi n}$  at 8 T, which is even smaller than  $\lambda$ . This implies that the  $k_F \propto \sqrt{n}$  is not valid for the charge carriers that participate in the interference, suggesting a constraint in motion for the 2D electron system. An effective 1D motion can arise if the charge carriers are already flowing in QH edge channels and remains unaffected by any further increase in the magnetic field. The absence of any periodic density oscillation in  $V_{xx}^{2\omega}$  at a low magnetic field also suggests that the trajectories only interfere in the QH regime. The valley-polarized chiral channels can be ignored as the possible origin of the thermopower oscillations because the displacement field is not strong enough ( $<0.1 \text{ V nm}^{-1}$ ) to induce a gap in the AB/BA regions, which provides the necessary topological protection.<sup>24,40</sup> Furthermore, we find that the magnitude of  $\Delta n$  is similar to that of  $n_g$ . This is remarkable because it reveals that the path difference between the interfering trajectories is much smaller than the area of the lithographically defined mtBLG channel ( $\sim \text{few } \mu\text{m}^2$ ), and comparable to the length scale of the moiré lattice.

Another modulation of the interference phase appears when we vary the magnetic field at constant doping. Figure 2d,e captures the thermovoltage oscillations with varying  $B$  at two different dopings. We observe the following: (1) The thermopower oscillations are periodic in  $B$  (Figure 2f). This is in stark contrast to the  $1/B$ -periodicity observed for Shubnikov–de Haas oscillations in 2D systems. The  $B$ -linear periodicity is consistent with AhB-oscillations when the

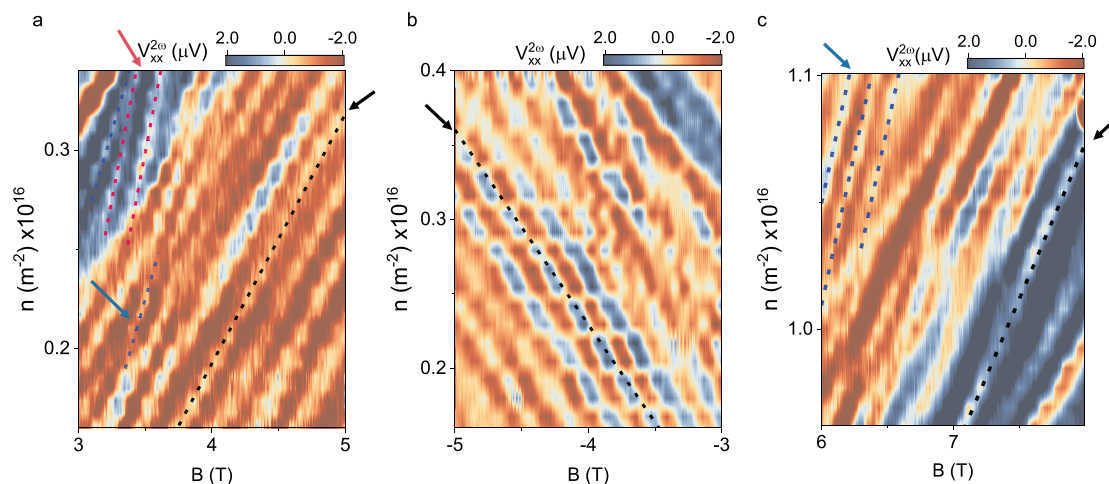


**Figure 3.** Interference patterns in  $n - B$  phase space at  $\nu = 4$ . Color plot of  $V_{xx}^{2\omega}$  in the  $n - B$  phase space at (a)  $\nu = +4$ , (b)  $\nu = -4$ , and (c)  $\nu = +4$  at higher doping and magnetic fields, respectively. The diagonal contrast shows the evolution of maxima/minima in the interference phase in the  $n - B$  phase space. The dashed lines show the magnitude of the slope  $\alpha \approx 1.24 \times 10^{15} \text{ m}^{-2} \text{ T}^{-1}$  (black),  $2\alpha$  (blue), and  $3\alpha$  (pink), respectively, as a guide to the eye.

interfering trajectories enclose a finite magnetic flux. We also find that the AhB-oscillations are symmetric with the direction of  $B$  (Figure 2d). This eliminates the possible role of contacts, spurious signals from the monolayer graphene heater and the transverse Hall component in the observed AhB-oscillations. (2) The oscillations only emerge at filling  $\nu = 4$  and 8 and diminish at higher order Landau levels. This is possibly because of a weak Landau level spectrum for  $\nu > 8$  because the gap becomes indiscernible in both  $R_{xx}$  and  $V_{xx}^{2\omega}$  in the experimental range of  $n$  and  $B$  (Figures 1b and 2a). The ubiquity of the AhB-oscillations at the lowest Landau levels in the  $n - B$  phase space indicates that the underlying mechanism of interference is profoundly connected to the formation of QH states in mtBLG. In contrast, the AhB-oscillations in the displacement field-driven helical states of mtBLG appear at very low magnetic fields and diminish at large magnetic fields.<sup>28</sup> For a spatially confined QH interferometer, changes in  $\nu$  correspond to changes in the Coulomb charging energy. An enhanced Coulomb interaction between the interfering Landau levels will result in an effective reduction of the area of the interferometer.<sup>13,38,41</sup> This leads to an increase in the periodicity of AhB-oscillations.<sup>38</sup> Rather surprisingly, we find that the periodicity ( $\Delta B \approx 250 \text{ mT}$ ) of the AhB-oscillations remains independent of the filling factor  $\nu$  (Figure 2f), suggesting diminished Coulomb charging effects between the charge carrier trajectories. From the periodicity of the AB phase,  $\phi_{AB} = BA_{\text{loop}}/\Phi_0$ , we estimate the enclosed loop area  $A_{\text{loop}} \approx 1.6 \times 10^{-14} \text{ m}^{-2}$ , which is exactly twice the area of the moiré unit cell ( $A_{\text{moiré}}$ ) and corroborates the results from the density-modulated oscillation shown in Figure 2b. Furthermore, we observe that the periodicity of AhB-oscillations remains unchanged ( $\Delta B \approx 240 \text{ mT}$ ) for the next nearest channel with similar  $\theta$  and channel length, suggesting that  $\Delta B$  depends only on the twist angle, i.e. the size of the moiré lattice (Figure S2, Supporting Information). This indicates that the interference area is intrinsic to the triangular domain structure of the moiré lattice across the mtBLG device and is not related

to any twist-angle inhomogeneity in the sample or parallel transport through the bulk.

We now turn to the results of  $V_{xx}^{2\omega}$  in the combined  $n - B$  phase space. Figure 3a,b illustrates the color map of  $V_{xx}^{2\omega}$  at  $|\nu| = 4$ . The loci of the constructive and destructive interference phases can be identified by the contrasting diagonal lines. The cumulative index  $j$  for the total interference phase can be described as

$$j = \frac{L_{\text{tot}}k_F}{2\pi} \pm \frac{A_{\text{loop}}B}{\Phi_0} \quad (2)$$

The spacing between the two constructive interference is  $\Delta j = \frac{L_{\text{tot}}\Delta k_F}{2\pi} \pm \frac{A_{\text{loop}}\Delta B}{\Phi_0} = 1$ . For AhB-oscillations in mtBLG, the phase associated with the path difference and the magnetic phase can be added in either a constructive or destructive way, which is equivalent to traversing the path in a clockwise or anticlockwise direction. This is captured by the both signs in eq 2.<sup>28</sup> However, we observe only positive slopes for the diagonal lines in the  $n - B$  phase space. This was further verified in the negative magnetic field at  $\nu = -4$  as shown in Figure 3b. We note that the observed positive sign of the slope is similar to the slope of the Landau fans emanating from the CNP. The absence of a negative slope in the  $n - B$  phase plane indicates that the motion of the charge carriers are allowed only in one direction, which is characteristically similar to the interference resulting from the QH states.<sup>3</sup> We also validate the positive slope of the constant-phase line at higher doping and magnetic fields but at the same Landau level  $\nu = 4$  (Figure 3c). The diagonal lines in the  $n - B$  phase space at  $|\nu| = 4$  reveal a primary slope  $\alpha \approx 1.24 \times 10^{15} \text{ m}^{-2} \text{ T}^{-1}$  (indicated by the black dashed lines in Figure 3a-c) along with weaker diagonal lines with slopes  $2\alpha$  (blue) and  $3\alpha$  (pink dashed lines). The latter correspond to higher harmonics of the same effective interfering area but different path length. Notably, varying  $V_{\text{tg}}$  in mtBLG changes the  $n(E_F)$  alone, which allows the observation of coupled oscillations in the  $n - B$  phase space

without changing the interference area, which is distinct from QH interferometers based on graphene<sup>15</sup> or GaAs systems.<sup>3,38</sup>

To elucidate the modulation of the interference phase in  $n$  and  $B$ , we propose the following. In the QH regime, the trajectories of the charge carriers are heavily influenced by the perpendicular magnetic field and the underlying moiré lattice. Because the domain walls separate the triangular AB/BA regions, the QH chiral channels will manifest along the domain walls (see Figure 4a) forming local Landau levels inside the

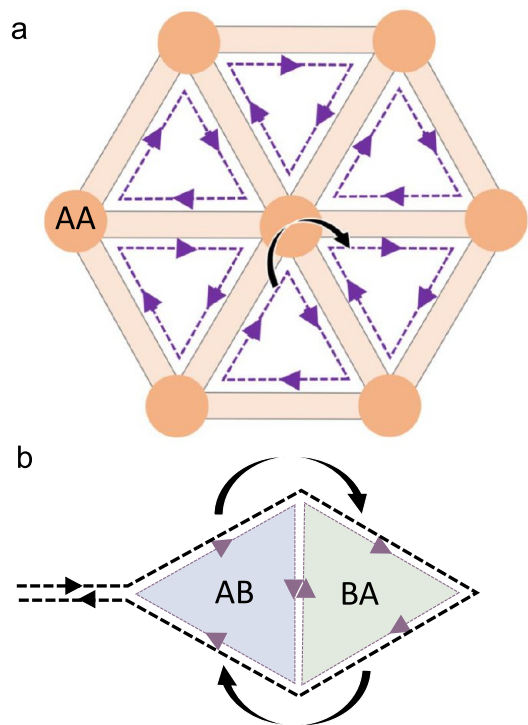


**Figure 4.** Interference of Quantum Hall (QH) states. (a) Schematic showing the formation of local Landau levels within the AB/BA domains in QH regime. The arrow shows tunneling or “hopping” between two neighboring local Landau levels facilitated by the AA-stacked regions. (b) Schematic showing an example of interference between two trajectories (black dashed lines) that enclose a finite magnetic flux through a moiré unit cell.

AB/BA domains.<sup>42,43</sup> Importantly, the domain walls function as a sample edge in the QH regime. The AA regions can function as nodes that facilitate tunneling between the local chiral edge channels of the neighboring AB/BA regions. The “hopping” of the charge carriers to neighboring QH channels gives rise to propagating modes that can carry charge and heat.<sup>44</sup> FP and AhB-oscillations can arise when the propagating modes interfere and enclose the finite magnetic flux as shown by the schematic in Figure 4b. This is conceptually similar to the formation of propagating zigzag channels and pseudo-Landau levels in mtBLG under a large vertical displacement field.<sup>44–47</sup> However, it is important to note that the interference associated with the QH channels is qualitatively different compared to that of the valley-polarized chiral channels. The latter only appears when the Fermi energy is within the displacement field-induced gap, while the former depends on the local Landau level formation within the AB/BA domains. Because any AA region can host hopping, this gives rise to the large number of the possible propagating modes, and the wave function of the charge carrier becomes

extended. This is contrary to the QH interference in GaAs systems, where the small area of the interferometer can only host a finite amount of charge, and the confinement effect plays a dominant role. We postulate that the extended nature of wave function leads to diminished Coulomb repulsion between the charge carrier even though the pseudo-Landau levels are localized within the domains. Furthermore, because only the AA-stacked regions can facilitate the hopping of charge carriers, the total scattering cross section is considerably reduced. This enables phase coherence between the propagating modes over the sample dimension.

Remarkably, we find that the maxima/minima diagonal lines in the  $n$ – $B$  phase space are linear to the variation of  $n$  and  $B$ . This suggests that, rather importantly, when the device is operated in the QH regime,  $k_F \sim n_{\text{QH}}$ , where  $n_{\text{QH}}$  is the 1D number density of charge carriers. This linear dependence is in stark contrast to the conventional 2D case, and can be attributed to the 1D motion of the charge carriers.  $n_{\text{QH}}$  can be estimated from the gate-induced number density ( $n$ ) using  $n_{\text{QH}} = n/N_{\text{ch}}$ , where  $N_{\text{ch}} = 2\sqrt{3}/\lambda$  is the density of edge channel per unit length (see Supporting Information for more details). Using  $n_{\text{QH}}$  in eq 2, we get  $L_{\text{tot}} = A_{\text{loop}} 2\sqrt{3} g / \alpha \lambda \Phi_0$ , where  $g$  is the degeneracy of the carriers. The experimentally obtained  $\alpha$  and  $A_{\text{loop}}$  renders  $L_{\text{tot}} \approx 450$  nm, which is  $\sim 4\lambda$ . However, the estimated  $L_{\text{tot}}$  is too small to enclose an area of  $A_{\text{loop}} \approx 1.6 \times 10^{-14} \text{ m}^{-2}$  ( $\approx \sqrt{3}\lambda^2$ ). This apparent discrepancy can be resolved when we consider the fact that all the charge carriers will be unlikely to participate in the 1D transport. Therefore, a fraction of charge carriers from the gate induced carrier density ( $n$ ) should manifest in the 1D density  $n_{\text{QH}}$ . This leads to an underestimation of  $L_{\text{tot}}$ . Although the extracted area  $A_{\text{loop}}$  ( $\approx 2A_{\text{moiré}}$ ) corresponds to a trajectory that encloses an effective area consisting of four AB/BA domains, the exact path length can manifest in many different geometries depending on the interference condition. We note that the minimum path length required to enclose  $A_{\text{loop}}$  is  $6\lambda$ , which corresponds to a triangular effective area; however, other trajectories are also possible. In the QH regime, each node (AA-stacked region) can support transfer of three incoming channels and three outgoing channels. This allows for different  $L_{\text{tot}}$  enclosing the same area.<sup>27</sup> We speculate that this leads to multiple harmonics in the observed slopes of the diagonal maxima/minima lines in the  $n$ – $B$  phase space in Figure 3a–c.

In conclusion, we have measured magneto-thermopower transport in a mtBLG sample with  $\theta \approx 0.16^\circ$ . We find periodic oscillations of thermovoltage in both  $n$  and  $B$  that is consistent with electronic FP and AhB interference between charge carrier trajectories that enclose a finite magnetic flux at a low temperature (3 K). The periodic oscillations could only be detected in thermovoltage measurements and not in conventional resistance measurements. The resonance patterns emerge only in the the QH regime at Landau fillings  $\nu = 4$  and 8, and persist throughout the different channels of the device. We estimate the enclosed loop area from the periodicity of AhB-oscillations, which is comparable to the moiré lattice size. Our observations indicate that charge carriers form local Landau levels within the AB/BA domains, and the neighboring QH modes interfere through AA regions. The intrinsic quantum Hall interference effect in mtBLG may act as a novel platform for realizing anyonic statistics in the fractional QH regime.

## ■ ASSOCIATED CONTENT

### SI Supporting Information

The Supporting Information is available free of charge at <https://pubs.acs.org/doi/10.1021/acs.nanolett.2c00627>.

Device fabrication and characterization, Electrical and thermoelectric measurements, Aharonov–Bohm oscillations in magneto-thermovoltage, and Fabry–Pérot oscillations in magneto-thermovoltage (PDF)

## ■ AUTHOR INFORMATION

### Corresponding Author

Phanibhusan S. Mahapatra – Department of Physics, Indian Institute of Science, Bangalore 560012, India; [orcid.org/0000-0002-1070-2116](https://orcid.org/0000-0002-1070-2116); Email: [phanis@iisc.ac.in](mailto:phanis@iisc.ac.in)

### Authors

Manjari Garg – Department of Instrumentation and Applied Physics, Indian Institute of Science, Bangalore 560012, India

Bhaskar Ghawri – Department of Physics, Indian Institute of Science, Bangalore 560012, India

Aditya Jayaraman – Department of Physics, Indian Institute of Science, Bangalore 560012, India; [orcid.org/0000-0002-6963-7195](https://orcid.org/0000-0002-6963-7195)

Kenji Watanabe – Research Center for Functional Materials, National Institute for Materials Science, Tsukuba, Ibaraki 305-0044, Japan; [orcid.org/0000-0003-3701-8119](https://orcid.org/0000-0003-3701-8119)

Takashi Taniguchi – International Center for Materials Nanoarchitectonics, National Institute for Materials Science, Tsukuba, Ibaraki 305-0044, Japan; [orcid.org/0000-0002-1467-3105](https://orcid.org/0000-0002-1467-3105)

Arindam Ghosh – Department of Physics, Indian Institute of Science, Bangalore 560012, India; Centre for Nano Science and Engineering, Indian Institute of Science, Bangalore 560012, India

U. Chandni – Department of Instrumentation and Applied Physics, Indian Institute of Science, Bangalore 560012, India

Complete contact information is available at:

<https://pubs.acs.org/doi/10.1021/acs.nanolett.2c00627>

### Author Contributions

P.S.M. contributed to the device fabrication, data acquisition, analysis and data interpretation. M.G. contributed in device fabrication and assisted in data acquisition. B.G. assisted in the analysis of the data. A.J. contributed in the data acquisition. U.C. and A.G. contributed in the data interpretation, and theoretical understanding of the paper. K.W. and T.T. synthesized the hBN single crystals. P.S.M., A.G., and U.C. contributed in writing the paper.

### Notes

The authors declare no competing financial interest.

## ■ ACKNOWLEDGMENTS

We gratefully acknowledge the usage of the MNCF and NNFC facilities at CeNSE, IISc. U.C. acknowledges funding from SERB through ECR/2017/001566. A.G. acknowledges financial support from the Department of Science and Technology (DST), Government of India. K.W. and T.T. acknowledge support from the Elemental Strategy Initiative conducted by the MEXT, Japan (Grant Number JPMXP0112101001) and JSPS KAKENHI (Grant Numbers 19H05790, 20H00354, and 21H05233).

## ■ REFERENCES

- (1) Nakamura, J.; Liang, S.; Gardner, G. C.; Manfra, M. J. Direct observation of anyonic braiding statistics. *Nat. Phys.* **2020**, *16*, 931–936.
- (2) Chamon, C. d. C.; Freed, D.; Kivelson, S.; Sondhi, S.; Wen, X. Two point-contact interferometer for quantum Hall systems. *Phys. Rev. B* **1997**, *55*, 2331.
- (3) Nakamura, J.; Fallahi, S.; Sahasrabudhe, H.; Rahman, R.; Liang, S.; Gardner, G. C.; Manfra, M. J. Aharonov–Bohm interference of fractional quantum Hall edge modes. *Nat. Phys.* **2019**, *15*, 563–569.
- (4) Das Sarma, S.; Freedman, M.; Nayak, C. Topologically protected qubits from a possible non-Abelian fractional quantum Hall state. *Phys. Rev. Lett.* **2005**, *94*, 166802.
- (5) Stern, A.; Halperin, B. I. Proposed experiments to probe the non-Abelian  $\nu = 5/2$  quantum Hall state. *Phys. Rev. Lett.* **2006**, *96*, 016802.
- (6) Kim, E.-A. Aharonov-Bohm interference and fractional statistics in a quantum Hall interferometer. *Phys. Rev. Lett.* **2006**, *97*, 216404.
- (7) Camino, F.; Zhou, W.; Goldman, V. Aharonov-Bohm electron interferometer in the integer quantum Hall regime. *Phys. Rev. B* **2005**, *72*, 155313.
- (8) Lin, P. V.; Camino, F.; Goldman, V. Electron interferometry in the quantum Hall regime: Aharonov-Bohm effect of interacting electrons. *Phys. Rev. B* **2009**, *80*, 125310.
- (9) Halperin, B. I. Statistics of quasiparticles and the hierarchy of fractional quantized Hall states. *Phys. Rev. Lett.* **1984**, *52*, 1583.
- (10) Halperin, B. I.; Stern, A.; Neder, I.; Rosenow, B. Theory of the Fabry–Pérot quantum Hall interferometer. *Phys. Rev. B* **2011**, *83*, 155440.
- (11) Von Keyserlingk, C.; Simon, S.; Rosenow, B. Enhanced bulk-edge Coulomb coupling in fractional Fabry–Perot interferometers. *Phys. Rev. Lett.* **2015**, *115*, 126807.
- (12) Gurman, I.; Sabo, R.; Heiblum, M.; Umansky, V.; Mahalu, D. Dephasing of an electronic two-path interferometer. *Phys. Rev. B* **2016**, *93*, 121412.
- (13) Ofek, N.; Bid, A.; Heiblum, M.; Stern, A.; Umansky, V.; Mahalu, D. Role of interactions in an electronic Fabry–Perot interferometer operating in the quantum Hall effect regime. *Proc. Natl. Acad. Sci.* **2010**, *107*, 5276–5281.
- (14) Bhattacharyya, R.; Banerjee, M.; Heiblum, M.; Mahalu, D.; Umansky, V. Melting of interference in the fractional quantum Hall effect: Appearance of neutral modes. *Phys. Rev. Lett.* **2019**, *122*, 246801.
- (15) Ronen, Y.; et al. Aharonov-Bohm effect in graphene-based Fabry–Pérot quantum Hall interferometers. *Nat. Nanotechnol.* **2021**, *16*, 563–569.
- (16) Willett, R. L.; Nayak, C.; Shtengel, K.; Pfeiffer, L. N.; West, K. W. Magnetic-field-tuned aharonov-bohm oscillations and evidence for non-abelian anyons at  $\nu = 5/2$ . *Phys. Rev. Lett.* **2013**, *111*, 186401.
- (17) Mills, S. M.; Averin, D. V.; Du, X. Localizing fractional quasiparticles on graphene quantum hall antidots. *Phys. Rev. Lett.* **2020**, *125*, 227701.
- (18) Mills, S. M.; Gura, A.; Watanabe, K.; Taniguchi, T.; Dawber, M.; Averin, D. V.; Du, X. Dirac fermion quantum Hall antidot in graphene. *Phys. Rev. B* **2019**, *100*, 245130.
- (19) Cao, Y.; Fatemi, V.; Demir, A.; Fang, S.; Tomarken, S. L.; Luo, J. Y.; Sanchez-Yamagishi, J. D.; Watanabe, K.; Taniguchi, T.; Kaxiras, E.; Ashoori, R. C.; Jarillo-Herrero, P. Correlated insulator behaviour at half-filling in magic-angle graphene superlattices. *Nature* **2018**, *556*, 80.
- (20) Cao, Y.; Fatemi, V.; Fang, S.; Watanabe, K.; Taniguchi, T.; Kaxiras, E.; Jarillo-Herrero, P. Unconventional superconductivity in magic-angle graphene superlattices. *Nature* **2018**, *556*, 43.
- (21) Sharpe, A. L.; Fox, E. J.; Barnard, A. W.; Finney, J.; Watanabe, K.; Taniguchi, T.; Kastner, M.; Goldhaber-Gordon, D. Emergent ferromagnetism near three-quarters filling in twisted bilayer graphene. *Science* **2019**, *365*, 605–608.

- (22) Yoo, H.; et al. Atomic and electronic reconstruction at the van der Waals interface in twisted bilayer graphene. *Nat. Mater.* **2019**, *18*, 448–453.
- (23) Huang, S.; Kim, K.; Efimkin, D. K.; Lovorn, T.; Taniguchi, T.; Watanabe, K.; MacDonald, A. H.; Tutuc, E.; LeRoy, B. J. Topologically protected helical states in minimally twisted bilayer graphene. *Phys. Rev. Lett.* **2018**, *121*, 037702.
- (24) San-Jose, P.; Prada, E. Helical networks in twisted bilayer graphene under interlayer bias. *Phys. Rev. B* **2013**, *88*, 121408.
- (25) Efimkin, D. K.; MacDonald, A. H. Helical network model for twisted bilayer graphene. *Phys. Rev. B* **2018**, *98*, 035404.
- (26) Walet, N. R.; Guinea, F. The emergence of one-dimensional channels in marginal-angle twisted bilayer graphene. *2D Mat* **2020**, *7*, 015023.
- (27) Xu, S. G.; Berdyugin, A. I.; Kumaravadeivel, P.; Guinea, F.; Krishna Kumar, R.; Bandurin, D. A.; Morozov, S. V.; Kuang, W.; Tsim, B.; Liu, S.; Edgar, J. H.; Grigorieva, I. V.; Fal'ko, V. I.; Kim, M.; Geim, A. K.; et al. Giant oscillations in a triangular network of one-dimensional states in marginally twisted graphene. *Nat. Commun.* **2019**, *10*, 1–5.
- (28) Rickhaus, P.; et al. Transport through a network of topological channels in twisted bilayer graphene. *Nano Lett.* **2018**, *18*, 6725–6730.
- (29) Mahapatra, P. S.; Ghawri, B.; Garg, M.; Mandal, S.; Watanabe, K.; Taniguchi, T.; Jain, M.; Mukerjee, S.; Ghosh, A. Misorientation-Controlled Cross-Plane Thermoelectricity in Twisted Bilayer Graphene. *Phys. Rev. Lett.* **2020**, *125*, 226802.
- (30) Izawa, K.; Behnia, K.; Matsuda, Y.; Shishido, H.; Settai, R.; Onuki, Y.; Flouquet, J. Thermoelectric response near a quantum critical point: The case of CeCoIn<sub>5</sub>. *Phys. Rev. Lett.* **2007**, *99*, 147005.
- (31) Barlas, Y.; Yang, K. Thermopower of quantum Hall states in Corbino geometry as a measure of quasiparticle entropy. *Phys. Rev. B* **2012**, *85*, 195107.
- (32) d'Ambrumenil, N.; Morf, R. Thermopower in the quantum hall regime. *Phys. Rev. Lett.* **2013**, *111*, 136805.
- (33) Yang, K.; Halperin, B. I. Thermopower as a possible probe of non-Abelian quasiparticle statistics in fractional quantum Hall liquids. *Phys. Rev. B* **2009**, *79*, 115317.
- (34) Dean, C.; et al. Hofstadter's butterfly and the fractal quantum Hall effect in moire superlattices. *Nature* **2013**, *497*, 598–602.
- (35) Ghawri, B.; Mahapatra, P. S.; Garg, M.; Mandal, S.; Bhowmik, S.; Jayaraman, A.; Soni, R.; Watanabe, K.; Taniguchi, T.; Krishnamurthy, H. R.; Jain, M.; Banerjee, S.; Chandni, U.; Ghosh, A.; et al. Breakdown of semiclassical description of thermoelectricity in near-magic angle twisted bilayer graphene. *Nat. Comm* **2022**, *13*, 1–7.
- (36) Jayaraman, A.; Hsieh, K.; Ghawri, B.; Mahapatra, P. S.; Watanabe, K.; Taniguchi, T.; Ghosh, A. Evidence of Lifshitz Transition in the Thermoelectric Power of Ultrahigh-Mobility Bilayer Graphene. *Nano Lett.* **2021**, *21*, 1221–1227.
- (37) Buhmann, J. M.; Sigrist, M. Thermoelectric effect of correlated metals: Band-structure effects and the breakdown of Mott's formula. *Phys. Rev. B* **2013**, *88*, 115128.
- (38) Zhang, Y.; McClure, D. T.; Levenson-Falk, E. M.; Marcus, C. M.; Pfeiffer, L. N.; West, K. W. Distinct signatures for Coulomb blockade and Aharonov-Bohm interference in electronic Fabry-Perot interferometers. *Phys. Rev. B* **2009**, *79*, 241304.
- (39) Handschin, C.; Makk, P.; Rickhaus, P.; Liu, M.-H.; Watanabe, K.; Taniguchi, T.; Richter, K.; Schonberger, C. Fabry-pérot resonances in a graphene/hbn moiré superlattice. *Nano Lett.* **2017**, *17*, 328–333.
- (40) Zhang, F.; MacDonald, A. H.; Mele, E. J. Valley Chern numbers and boundary modes in gapped bilayer graphene. *Proc. Natl. Acad. of Sci.* **2013**, *110*, 10546–10551.
- (41) Rosenow, B.; Halperin, B. Influence of interactions on flux and back-gate period of quantum Hall interferometers. *Phys. Rev. Lett.* **2007**, *98*, 106801.
- (42) Baßler, N. S.; Schmidt, K. P. Effects of domain walls in bilayer graphene in an external magnetic field. *Phys. Rev. B* **2021**, *103*, 155422.
- (43) Kisslinger, F.; Ott, C.; Heide, C.; Kampert, E.; Butz, B.; Spiecker, E.; Shallcross, S.; Weber, H. B. Linear magnetoresistance in mosaic-like bilayer graphene. *Nat. Phys.* **2015**, *11*, 650–653.
- (44) De Beule, C.; Dominguez, F.; Recher, P. Aharonov-Bohm Oscillations in Minimally Twisted Bilayer Graphene. *Phys. Rev. Lett.* **2020**, *125*, 096402.
- (45) Ramires, A.; Lado, J. L. Electrically tunable gauge fields in tiny-angle twisted bilayer graphene. *Phys. Rev. Lett.* **2018**, *121*, 146801.
- (46) Tsim, B.; Nam, N. N.; Koshino, M. Perfect one-dimensional chiral states in biased twisted bilayer graphene. *Phys. Rev. B* **2020**, *101*, 125409.
- (47) Fleischmann, M.; Gupta, R.; Wullschlager, F.; Theil, S.; Weckbecker, D.; Meded, V.; Sharma, S.; Meyer, B.; Shallcross, S. Perfect and controllable nesting in minimally twisted bilayer graphene. *Nano Lett.* **2020**, *20*, 971–978.

## Recommended by ACS

### Structural Reconstruction of Optically Invisible State in a Single Molecule via Scanning Tunneling Microscope

Guohui Dong, Hui Dong, et al.

OCTOBER 08, 2021  
THE JOURNAL OF PHYSICAL CHEMISTRY LETTERS

READ 

### Confined Vacuum Resonances as Artificial Atoms with Tunable Lifetime

Rasa Rejali, Sander Otte, et al.

JULY 11, 2022  
ACS NANO

READ 

### Anyonic Two-Photon Statistics with a Semiconductor Chip

Saverio Francesconi, Sara Ducci, et al.

AUGUST 31, 2021  
ACS PHOTONICS

READ 

### Ab Initio Properties of Hybrid Cove-Edged Graphene Nanoribbons as Metallic Electrodes for Peptide Sequencing via Transverse Tunneling Current

Giuseppe Zollo and Tommaso Civitarese

JULY 14, 2022  
ACS OMEGA

READ 

Get More Suggestions >